REPORT DOCUMENTATION PAGE

Form Approved OMB NO. 0704-0188

1. REPORT DATE (DD-MM-YYYY)	2. REPORT TYPE	3. DATES COVERED (From - To)
05-08-2015	Final Report	31-Jan-2014 - 30-Apr-2015

4. TITLE AND SUBTITLE
Final Report: "Superconducting Qubit Optical Transducer" (SQOT)

5a. CONTRACT NUMBER

5b. GRANT NUMBER
W911NF-14-C-0041

5c. PROGRAM ELEMENT NUMBER

6. AUTHORS
Colm Ryan, Hanhee Paik

5d. PROJECT NUMBER

5e. TASK NUMBER

5f. WORK UNIT NUMBER

7. PERFORMING ORGANIZATION NAMES AND ADDRESSES
Raytheon BBN Technologies Corp.
10 Moulton Street

Cambridge, MA 02138 -1119

8. PERFORMING ORGANIZATION REPORT NUMBER

9. SPONSORING/MONITORING AGENCY NAME(S) AND ADDRESS (ES)
U.S. Army Research Office
P.O. Box 12211
Research Triangle Park, NC 27709-2211

10. SPONSOR/MONITOR'S ACRONYM(S)
ARO

11. SPONSOR/MONITOR'S REPORT NUMBER(S)
64448-PH-OC.1

12. DISTRIBUTION AVAILABILITY STATEMENT
Approved for Public Release; Distribution Unlimited

13. SUPPLEMENTARY NOTES
The views, opinions and/or findings contained in this report are those of the author(s) and should not contrued as an official Department of the Army position, policy or decision, unless so designated by other documentation.

14. ABSTRACT
The SQOT (Superconducting Qubit Optical Transducer) project proposes to build a novel electro-optic system which can exchange quantum information between optical qubits at telecom frequencies and superconducting qubits. A direct quantum information transfer between optical qubits and superconducting qubits has not yet been demonstrated. Our scheme is to use high-Q (quality factor) three-dimensional (3D) superconducting qubits fabricated on a nonlinear electro-optic material that forms a high-Q whispering gallery optical cavity. The high

15. SUBJECT TERMS
SQOT Final Report

16. SECURITY CLASSIFICATION OF:			17. LIMITATION OF ABSTRACT	15. NUMBER OF PAGES	19a. NAME OF RESPONSIBLE PERSON
a. REPORT	b. ABSTRACT	c. THIS PAGE			Hanhee Paik
UU	UU	UU	UU		19b. TELEPHONE NUMBER 617-873-8028

Standard Form 298 (Rev 8/98)
Prescribed by ANSI Std. Z39.18

Report Title

Final Report: "Superconducting Qubit Optical Transducer" (SQOT)

ABSTRACT

The SQOT (Superconducting Qubit Optical Transducer) project proposes to build a novel electro-optic system which can exchange quantum information between optical qubits at telecom frequencies and superconducting qubits. A direct quantum information transfer between optical qubits and superconducting qubits has not yet been demonstrated. Our scheme is to use high-Q (quality factor) three-dimensional (3D) superconducting qubits fabricated on a nonlinear electro-optic material that forms a high-Q whispering gallery optical cavity. The high quality factors will be essential to achieve coherent quantum behavior, in contract to similar systems in the classical regime. The initial one-year effort proposed here will explore the cryogenic behavior of the nonlinear material and optical components necessary to build SQOT for our direct coupling scheme; and measure the coherent coupling coefficient between optical and superconducting qubits with SQOT, which we expect g~10kHz and in the fully quantum coherent regime.

Enter List of papers submitted or published that acknowledge ARO support from the start of the project to the date of this printing. List the papers, including journal references, in the following categories:

(a) Papers published in peer-reviewed journals (N/A for none)

Received Paper

TOTAL:

Number of Papers published in peer-reviewed journals:

(b) Papers published in non-peer-reviewed journals (N/A for none)

Received Paper

TOTAL:

Number of Papers published in non peer-reviewed journals:

(c) Presentations

Number of Presentations: 0.00

Non Peer-Reviewed Conference Proceeding publications (other than abstracts):

Received Paper

TOTAL:

Number of Non Peer-Reviewed Conference Proceeding publications (other than abstracts):

Peer-Reviewed Conference Proceeding publications (other than abstracts):

Received Paper

TOTAL:

Number of Peer-Reviewed Conference Proceeding publications (other than abstracts):

(d) Manuscripts

Received Paper

TOTAL:

Number of Manuscripts:

Books

Received Book

TOTAL:

Received Book Chapter

TOTAL:

Patents Submitted

Patents Awarded

Awards

Graduate Students

NAME	PERCENT_SUPPORTED
FTE Equivalent:	
Total Number:	

Names of Post Doctorates

NAME	PERCENT_SUPPORTED
FTE Equivalent:	
Total Number:	

Names of Faculty Supported

NAME PERCENT_SUPPORTED

FTE Equivalent:
Total Number:

Names of Under Graduate students supported

NAME PERCENT_SUPPORTED

FTE Equivalent:
Total Number:

Student Metrics

This section only applies to graduating undergraduates supported by this agreement in this reporting period

The number of undergraduates funded by this agreement who graduated during this period:	0.00
The number of undergraduates funded by this agreement who graduated during this period with a degree in science, mathematics, engineering, or technology fields:	0.00
The number of undergraduates funded by your agreement who graduated during this period and will continue to pursue a graduate or Ph.D. degree in science, mathematics, engineering, or technology fields:	0.00
Number of graduating undergraduates who achieved a 3.5 GPA to 4.0 (4.0 max scale):	0.00
Number of graduating undergraduates funded by a DoD funded Center of Excellence grant for Education, Research and Engineering:	0.00
The number of undergraduates funded by your agreement who graduated during this period and intend to work for the Department of Defense	0.00
The number of undergraduates funded by your agreement who graduated during this period and will receive scholarships or fellowships for further studies in science, mathematics, engineering or technology fields:	0.00

Names of Personnel receiving masters degrees

NAME

Total Number:

Names of personnel receiving PHDs

NAME

Total Number:

Names of other research staff

NAME PERCENT_SUPPORTED

FTE Equivalent:
Total Number:

Sub Contractors (DD882)

Inventions (DD882)

Scientific Progress

See Attachment

Technology Transfer

Raytheon
BBN Technologies

BBN Technologies
10 Moulton Street
Cambridge, MA 02138

5 August 2015

US Army Research Office
Attn: RDRL-ROS-I (Reports)
PO Box 12211
Research Triangle Park, NC 27709-2211

Delivered via US Army Extranet and Email to:
https://extranet.aro.army.mil
USarmy.rtp.aro.mbx.reports@mail.mil
andrew.day.civ@mail.mil

Contract Number:	W911NF-14-C-0041
Proposal Number:	P13089-BBN
Contractor Name and PI:	Raytheon BBN Technologies; Dr. Colm Ryan
Contractor Address:	10 Moulton Street, Cambridge, MA 02138
Title of the Project:	Superconducting Qubit Optical Transducer (SQOT)
Contract Period of Performance:	31 January 2014 – 30 April 2015
Total Contract Amount:	$784,306
Amount of Funds Paid by DFAS to date:	$784,306
Total Amount Expended to date (thru fiscal October):	$784,306
Number of Employees working on the project:	6
Number of New Employees placed on contract:	0
Report Period Covering:	31 January 2014 – 30 April 2015

Attention: Mr. Andrew Day
Subject: Final Report
Reference: Section F, Clause F.2 Deliverables

In accordance with reference requirement of the subject contract, Raytheon BBN Technologies (BBN) hereby submits its' Final Report. This cover sheet and enclosure have been distributed in accordance with the contract requirements.

Please do not hesitate to contact Dr. Colm Ryan at 617.873.8163 (email: cryan@bbn.com) should you wish to discuss any technical matter related to this report, or contact the undersigned, Ms. Kathryn Carson at 617.873.8144 (email: kcarson@bbn.com) if you would like to discuss this letter or have any other questions.

Sincerely,
Raytheon BBN Technologies

Kathryn Carson

Program Manager

RAYTHEON BBN TECHNOLOGIES AND IBM

SQOT Final Technical Report

Colm Ryan and Hanhee Paik

August 5, 2015

CONTENTS

1 Project Objectives

The superconducting qubit optical transducer (SQOT) program explored the feasibility of bi-directional conversion between optical photons ($\approx 1.5\mu$m) and microwave ($\approx$ 10GHz) photons using the intrinsic electro-optic coefficient of $LiNbO_3$. This material is commonly used in room-temperature electro-optic modulators and the SQOT program investigated the feasibility of migrating this technology to a device with high enough conversion efficiency to be useful for quantum information and be compatible with dilution fridge technologies and integration with superconducting qubits. In particular the SQOT program attempted to answer:

- The transient dynamics of the entanglement process and expected entanglement generation fidelity;
- Numerical calculation of the expected microwave-optical mode overlap and bare microwave-optical coupling rate;
- The cryogenic properties of $LiNbO_3$ and its compatibility with long coherence time superconducting circuits;
- The feasibility of fabrication of microwave superconducting circuits directly on $LiNbO_3$;
- The design of a cryogenically compatible optical coupling to a very high Q traveling wave resonator.

2 Theory Work

2.1 Interconversion Hamiltonian

The SQOT device is a concrete implementation of a proposed device to overlap a microwave and optical resonator on an electro-optic material [1, 2]. The electro-optic material naturally couples the microwave and optical electric fields as the application of an microwave electric field shifts the optical index of refraction. Jumping directly to a quantum description, consider a family of optical resonator modes a_k separated by the free spectral range (FSR) and a microwave mode b, the total Hamiltonian is:

$$H = \omega_a a_0^\dagger a_0 + (\omega_a - \mathrm{FSR})\, a_{-1}^\dagger a_{-1} + (\omega_a - 2\mathrm{FSR})\, a_{-2}^\dagger a_{-2} + \\ \omega_b b^\dagger b + g\left(b + b^\dagger\right)(a_0 + a_{-1} + a_{-2})\,(a_0 + a_{-1} + a_{-2})^\dagger \quad (2.1)$$

where g is the bare electro-optic coupling (see section 2.3). Moving into an interaction frame and making the conventional rotating-frame approximation we end up with three-mode interaction between two optical modes and the microwave mode. If we then pump one of the optical modes we can replace the pumped mode's, field operators with classical complex amplitudes and we have parameterically driven interconversion or downconversion with a rate that depends on the square root of the number of pump photons N:

$$H_I = \sqrt{N} g \left[\left(a_0^\dagger b + a_0 b^\dagger\right) + \left(a_{-2} b + a_2^\dagger b^\dagger\right)\right] \quad (2.2)$$

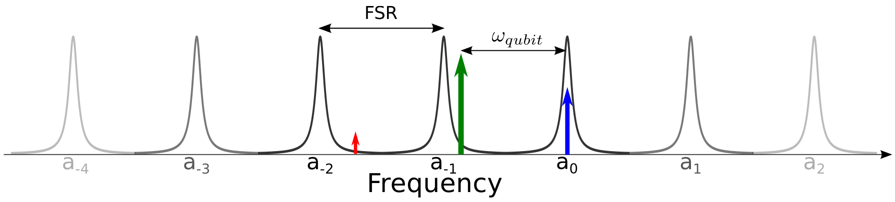

Figure 2.1: Optical modes of the SQOT device. Pumping slightly off-resonance (green tone) enables up-conversion (inter-conversion) but suppresses the parasitic down-conversion.

When the microwave mode is detuned from the FSR we can tune between the two types of operation through the pump tone frequency. As show in Figure 2.1 the relative efficiency of the two processes depends on the alignment of the particular sideband with the optical modes' density of states. This gives us an important experimental tunability: there will be some spread in the qubit's frequency from fabrication variance however we can compensate with a tunable pump laser. The limit to the tunability is that we cannot be too far off-resonance or we will not get a sufficient number of pump photons into the resonator.

The bare electro-optic coupling is far too weak to allow quantum interconversion so it must be enhanced in two ways:

1. The effective interaction strength is scaled with the square root of the number of pump photons ($\sqrt{N}$). However, this could be limited by a number of factors:
   a) the cooling power of the dilution fridge;
   b) non-linearities in the $LiNbO_3$ material;
   c) scattering of photons destroying the coherence or even superconductivity of the microwave circuits;
   d) the requirement to modulate the interaction (see below).
2. The effective interaction length is increased by the microwave and optical resonators as the photons spend additional time before leaking out of the resonators.

The interconversion efficiency will be limited by the fastest resonator's decay rate. Since the optical frequency is so much larger than the microwave this puts stringent demands on the Q of the optical resonator. Assuming a pumped coupling rate of 1MHz we need an optical linewidth much less than this. For 1.5μm light (200THz) this implies a $Q > 10^8$. This design requirement pushes us to traveling-wave resonators such as whispering gallery mode disk resonators. The high optical Q also helps ameliorate some of the pumping power issues by reducing the photon scattering and power dissipation and decreasing the input power required. However, as we will see below it will be helpful to modulate the interaction for pulse shaping purposes and a high Q will make this challenging.

2.2 Qubit-Photon Entanglement

The parametric interaction enables interconversion between the microwave and optical cavities but to make this a useful device for distributing quantum entanglement we need to consider the traveling optical mode leaking out of the cavity and how to capture the quantum information in it. Previous demonstrations [3] have considered only the steady-state response which although necessary is not suffiicent to demonstrate entanglement.

2.2.1 System Equations of Motion

Consider the Langevin equations of motion for the mode operators in a SQOT-like device after moving to the strongly pumped parametric regime. We have a 2-level artificial atom (e.g. a transmon superconducting circuit) interacting with the field in an optical cavity, which in turn is coupled to a single (spatial) mode transmission line. The atom-cavity interaction is given by a Jaynes-Cummings Hamiltonian $\hat{H}_{\mathrm{JC}} = ab^{\dagger} + a^{\dagger}b$ of tunable strength $g(t)$, while the coupling κ between the cavity and the transmission line is assumed to be fixed in time. The equations of motion in the rotating frame of the system are given by

$$\dot{\hat{a}} = -\mathrm{i}\,g(t)[\hat{a}, \hat{H}_{\mathrm{JC}}] - \frac{\kappa}{2}\hat{a} + \sqrt{\kappa}\hat{c}_{\mathrm{in}}, \tag{2.3}$$

$$\dot{\hat{b}} = -\mathrm{i}\,g(t)[\hat{b}, \hat{H}_{\mathrm{JC}}], \tag{2.4}$$

where $\hat{a}$ is the cavity field annihilation operation, $\hat{b}$ is the lowering operator for the atom, and $\hat{c}_{\mathrm{in}}$ is the input field from the transmission line (we choose units where $\hbar = 1$).

The fields obey the cannonical input-output relations so that, by solving for $\hat{a}(t)$ and using some given joint state for the cavity and the input mode,

$$\hat{c}_{\mathrm{out}} - \hat{c}_{\mathrm{in}} = \sqrt{\kappa}\hat{a}, \tag{2.5}$$

so that, by solving for $\hat{a}(t)$ using some given joint state for the cavity and the input mode (conventionally assuming the input field is in the vacuum state), we may compute properties of the output field.

2.2.2 Microwave → Optical Conversion

For most of the work we consider a particular experiment driven by the milestone of the SQOT program to observe entanglement between a qubit and optical photon and similar to experiments demonstrated solely in the microwave domain [4]:

1. Start with the system in ground state.
2. Apply a π pulse on the qubit to take it to the first excited state.
3. Turn on the pump to apply the interconversion Hamiltonian (2.2) and turn off the pump half-way through the swap operation to create Bell pair entangled state between the microwave and optical cavity.

4. Let the optical state leak out of the cavity.

5. Measure the correlations between the qubit and

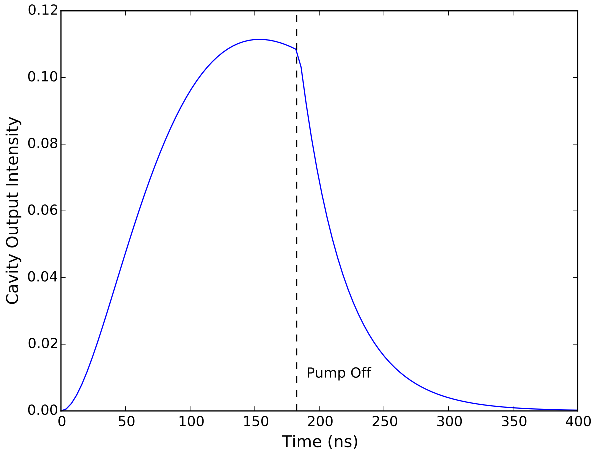

Figure 2.2: Average output intensity from a qubit-photon entanglement simulation without loss. Other parameters: $g = 1$kHz; $\omega_b = 10$GHz; $\Delta b = 300$MHz (qubit anharmonicity); $Q = 2 \times 10^7$; $N = 9.7 \times 10^5$; $\delta = 2$MHz (pump detuning).

We can immediately see that we are in an intermediate coupling regime where the optical photon is leaking out as it is being converted from the microwave. The shape is significantly different to a simple decaying exponential and so some additional effort has to be expended to full capture the information.

PULSE SHAPING If we consider a network of SQOT devices then we may want to consider how to reverse this process: capture an optical photon and faithfully convert its state to a microwave photon. To see how this works one can consider a time reversal of the above microwave → optical process above. Clearly to get perfect absorption of the outgoing photon in a second SQOT device we need to time-reverse the pulse. Since optical pulse time reversal is difficult, a workaround is to have a time-symmetrical pulse shape. We can achieve this through modulation of the pump field.

ROBUSTNESS TO PHOTON LOSS An additional issue that became clear in the SQOT work is that current microwave-optical interconversion approaches have not been made robust to optical photon loss. The atom-photon entanglement work has focused on making their networks robust by requiring “that quantum information is not encoded in the presence of a photon, but in its polarization, path, frequency, or arrival time."[5]. The atomic systems used have a rich atomic level structure that affords two niceties not yet available in the microwave interconversion physics:

- Multiple decay paths that couple to different polarizations.
- Heralded absorption in a second conversion device allows the post-selection of successful send and receive events such that losses can be treated as erasure errors rather than relaxation.

This issue appears to preclude the possibility of a send and receive type entanglement generation has photon loss in the optical fibre would appear has an effective T_1 process and destroy any entanglement.

2.2.3 Temporal Mode Filter Function

To get at all the information in the outgoing optical photon we need to match its temporal mode. The temporal mode annihilation operator is given by

$$\hat{C} = \int_0^\infty \mathrm{d}t\, f_C(t)\; \hat{c}_{\mathrm{out}}(t) \tag{2.6}$$

where $f_C(t)$ is a mode function that satisfies $\int_0^\infty \mathrm{d}t\,|f_C(t)|^2 = 1$ so that, in conjunction with the free field commutation relations $[\hat{c}_{\mathrm{out}}(t_1), \hat{c}^\dagger_{\mathrm{out}}(t_2)] = \delta(t_1 - t_2)$, it implies that $[\hat{C}, \hat{C}^\dagger] = 1$. In principle, we have arbitrary freedom in defining $f_C(t)$, but we clearly want to optimize it so that it is best matched to the output of the cavity for some chosen state transfer protocol. Once this $f_C(t)$ is chosen, we would like to reconstruct the joint state of the corresponding temporal mode and the atom *after* some interaction that is mediated by the cavity through the modulation of $g(t)$.

Ideally we would like to choose the temporal mode that captures all radiation leaking out of the cavity. This is only possible of the output of the cavity is indeed single mode. This can be verified straightforwardly by computing the correlation function

$$G(t_1, t_2) = \langle \hat{c}^\dagger_{\mathrm{out}}(t_1)\hat{c}_{\mathrm{out}}(t_2)\rangle, \tag{2.7}$$

and noticing that the Mercer's theorem guarantees that, under mild conditions on G, one can define $f_k(t)$ for $t \in [0,\infty)$ such that

$$\int_0^\infty \mathrm{d}t\, f_k^*(t) f_j(t) = \delta_{kj} \tag{2.8}$$

and

$$G(t_1, t_2) = \sum_{k=1}^{\infty} \langle \hat{n}_k\rangle f_k^*(t_1) f_k(t_2), \tag{2.9}$$

with $\langle \hat{n}_k\rangle \geq 0$ (without loss of generality, we choose the n_k to be in non-increasing order). Defining

$$\hat{C}_k = \int_0^\infty \mathrm{d}t\, f_k(t)\; \hat{c}_{\mathrm{out}}(t), \tag{2.10}$$

we obtain the intuitive results that

$$\hat{c}_{\text{out}} = \sum_k \hat{C}_k, \tag{2.11}$$

$$\langle \hat{n}_k \rangle = \langle \hat{C}_k^\dagger \hat{C}_k \rangle, \tag{2.12}$$

$$\sum_k \langle \hat{n}_k \rangle = \int_0^\infty \mathrm{d}t\, G(t,t), \tag{2.13}$$

and therefore a field has a single temporal mode if and only if $G(t_1,t_2) \propto f_1^*(t_1) f_1(t_2)$.

If the cavity and the input field are in the ground state, then arbitrary states of the 2-level "qubit" are guaranteed to lead to single temporal-mode fields at the output.

Extraction of non-classical cavity states Considering the correlation matrix of the outgoing radiation as defining the temporal mode structure leads to a simple example of a non-classical state that does not decay into a single temporal mode function: a n photon Fock state where $n > 1$. To achieve an n photon Fock state in a single temporal mode would require deliberate modulation of the cavity-free field coupling [6].

2.2.4 State Reconstruction

Given the mode operators for the outgoing temporal mode we can then define a density matrix for the joint qubit-photon state.The density matrix corresponding to this joint state can be inferred from the correlations

$$\langle (b^\dagger)^{m_1} b^{m_2} (C^\dagger)^{n_1} C^{n_2} \rangle, \tag{2.14}$$

where $b = b(\tau)$ for some particular τ after the atom-cavity interaction has been turned off. These are precisely the types of correlations that can be measured naturally by measuring the atom and the temporal mode independently, which implicitly assumes that the operators on each subsystem commute. Commutation also ensures that the operators $(b^\dagger)^{m_1} b^{m_2} (C^\dagger)^{n_1} C^{n_2}$ generate the relevant matrix algebra for the joint system.

Assuming that we have at most a single excitation in the system, and given we have a 2-level atom, it suffices to consider $m_i, n_i \leq 1$, leading to $2^4 - 1 = 15$ non-trivial correlations (analogously, one can think of pseudo-spin Pauli operators acting on the joint system, and compute slightly different correlations).

As stated, the sufficiency of these correlation for reconstruction hinges on the additional assumption that $[b, C] = [b, C^\dagger] = 0$, i.e., that the atom and the temporal mode in question can be considered as independent subsystems. Recall, however, that these commutation relations are not true for all choices of temporal mode, since

$$[\hat{b}(t_1), \hat{c}_{\text{out}}(t_2)] = u(t_2 - t_1)\sqrt{\kappa}[\hat{b}(t_1), \hat{a}(t_2)], \tag{2.15}$$

$$u(t) = \begin{cases} 1, & t > 0 \\ \frac{1}{2}, & t = 0 \\ 0, & t < 0 \end{cases}, \tag{2.16}$$

which follows from causality considerations.

2.2.5 Modified Temporal Modes

Despite qubit states of the atom leading to single temporal-mode states of the output field, the operators for this single mode generally do not commute with the atom operators. This greatly complicates how the joint atom-field state may be reconstructed, as the measurements that are accessible in an experiments are largely restricted to correlations of the form give by (2.14), which require commutativity in order to be experimentally accessible.

This problem can be solved by choosing some other mode $\hat{C}$ such that $[\hat{b}, \hat{C}] = [\hat{b}, \hat{C}^\dagger] = 0$. Since the single mode at the output of the cavity does not commute with $\hat{b}$, this necessarily implies that a commuting mode cannot be perfectly matched to the output of the cavity. Despite this mismatch, we will now consider only the joint state between the atom and this commuting temporal mode, and will return to the overall state of the system later.

The mode operator $\hat{C}$ commuted with $\hat{b}$ if and only if

$$\int_0^\infty \mathrm{d}t\, f_C(t) u(t-\tau)[\hat{b}(\tau), \hat{a}(t)] = 0, \tag{2.17}$$

$$\int_0^\infty \mathrm{d}t\, f_C(t) u(t-\tau)[\hat{b}(\tau), \hat{a}^\dagger(t)] = 0, \tag{2.18}$$

but these considtions are generally hard to enforce since the commutators are hard to obtain analytically. Instead we may require that

$$\int_0^\infty \mathrm{d}t\, f_C(t) u(t-\tau)\langle[\hat{b}(\tau), \hat{a}(t)]\rangle = 0, \tag{2.19}$$

$$\int_0^\infty \mathrm{d}t\, f_C(t) u(t-\tau)\langle[\hat{b}(\tau), \hat{a}^\dagger(t)]\rangle = 0, \tag{2.20}$$

for all initial states of interest. In our case, the input field and the cavity are taken to be in the vacuum states, so that from a choice of linearly independent input states that span the space of density operators for the atom, one can then simply choose $f_C(t)$ to be orthogonal to the space spanned by the different $\langle[\hat{b}(\tau), \hat{a}(t)]\rangle$ and $\langle[\hat{b}(\tau), \hat{a}^\dagger(t)]\rangle$. More specifically, let

$$p_{\perp,i}(t) = \langle[\hat{b}(\tau), \hat{a}^\dagger(t)]\rangle_{\hat{\sigma}_i}, \tag{2.21}$$

$$q_{\perp,i}(t) = \langle[\hat{b}(\tau), \hat{a}^\dagger(t)]\rangle_{\hat{\sigma}_i}, \tag{2.22}$$

where the $\hat{\sigma}_i$ for an informationally complex set of atom states, and let $\mathscr{P}^\perp$ be the projector onto the span of all $p_{\perp,i}(t)$ and $q_{\perp,i}(t)$. Then $f_C(t) \propto \mathscr{P} f_1(t) = f_1(t) - \mathscr{P}^\perp f_1(t)$, with the constant of proportionality chosen to give the proper mode normalization, corresponds to the optimal commuting temporal mode.

2.2.6 Entanglement

We consider the particular scenario where we start with a single excitation in the atom, drive the interaction at a constant strength $g_{\text{eff,max}}$ for some time, and then turn off the interaction. If the interaction time is appropriately chosen, and intrinsic losses are ignored, the state of the atom should be maximally entangled with the state of the output field (once we let all excitations in the cavity decay). Figure 2.3 shows how the entanglement degrades when we consider the joint state of the atom and the commuting temporal mode, both in the idealized lossless case, as well as in the case where intrinsic losses are considered. For the lossy case, we took $\Gamma_b/\kappa \approx \Gamma_a/\kappa \approx 0.2$.

As the results indicate, entanglement is most easily observed when $g_{\text{eff,max}} \gg \kappa$, and the degradation in observed entanglement is dominated by the mode-mismatch between the cavity output and the commuting temporal mode. Despite all this, entanglement remains observable even κ is significantly larger than $g_{\text{eff,max}}$.

2.3 Numerical Calculation of Mode Overlap

2.3.1 Coupling Rate Equations

The optical-microwave coupling is driven by the overlap between the two optical and one microwave modes involved in the parametric process [7]. We can simplify the overlap integral by considering a single dimension. This assumption is particularly valid in the case of $LiNbO_3$ where electro-optic coefficient is large along only one axis. Taking this to be the Z-direction from a z-cut wafer then the interaction energy U is

$$g = \frac{n^4}{4\pi}\int_V dv\, r_{33} E_{1z} E_{2z} E_z \tag{2.23}$$

where n is the optical index of refraction, r_{33} is the electro-optic coefficient along the z direction, $E_{1/2z}$ the optical electric fields and E_z the microwave electric field. We can then pull out the spatial dependence from the prefactors by defining normalized modes Φ

$$E_{1z} = i\sqrt{\frac{2\pi\hbar\omega_1}{n_e^2 V_a}}\left(a\Phi_a - a^\dagger\Phi_a^*\right) \tag{2.24}$$

$$E_{2z} = i\sqrt{\frac{2\pi\hbar\omega_2}{n_e^2 V_b}}\left(b\Phi_b - b^\dagger\Phi_b^*\right) \tag{2.25}$$

$$E_{z} = i\sqrt{\frac{2\pi\hbar\omega_m}{n_m^2 V_m}}\left(c\Phi_c - c^\dagger\Phi_c^*\right) \tag{2.26}$$

where the spatial functions Ψ are normalized to their respective mode volumes such that $\int_V dv|\Phi_k|^2 = V_k$. Having done that, the optical-microwave coupling breaks into two parts: $g = g_0\xi$ where g_0 is the maximum coupling achievable and ξ gives a mode overlap and phase matching scaling.

$$g_0 = \omega_{opt.} r_{33}\frac{n_e^2}{2}\sqrt{\frac{2\pi\hbar\omega_m}{n_m^2 V_m}} \tag{2.27}$$

and

$$\xi = \frac{1}{\sqrt{V_a V_b}}\left|\int_V dv\,\Phi_a\Phi_b^*\Phi_c^*\right| \tag{2.28}$$

A few key points are highlighted by the equations:

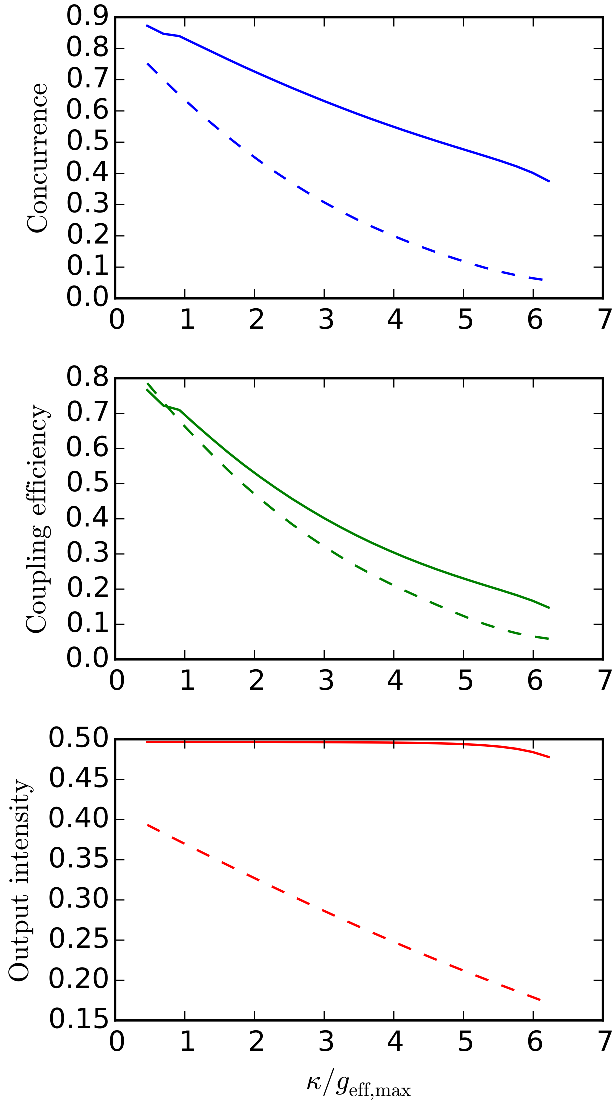

Figure 2.3: Entanglement between the atom and the commuting mode as a function of $\kappa/g_{\text{eff,max}}$. Solid lines correspond to the lossless regime, with the dashed line corresponds to non-zero intrinsic losses in the atom and in the cavity. We can see that, due to poor matching between the commuting mode and the output of the cavity, the atom-mode entanglement degrades as κ becomes comparable to $g_{\text{eff,max}}$, although it remains non-zero even when κ is significantly larger than $g_{\text{eff,max}}$.

Design	Mode Volume (m^{-3})	Frequency (GHz)	Max. Coupling Rate (kHz)
Dipole	5.2×10^{-14}	5.22	7.8
Dipole with Ground Plane	4.5×10^{-13}	8.02	3.3
C-Dipole	1.3×10^{-14}	6.82	18.1
Sectioned Dipole	2.7×10^{-13}	13.47	5.6
Flip-chip dipole	3.9×10^{-14}	4.84	8.7
Oar qubit	5.8×10^{-16}	6.88	84.9
Microstrip ring	3.9×10^{-13}	12.53	4.5
Coax cavity	1.4×10^{-12}	13.03	2.3

Table 2.1: Mode volumes, frequencies and maximum achievable couplings for 8 different SQOT devices. The final two simulations were linear microwave resonators without a Josephson junction for reference. These coupling rates will be reduced by imperfect phase matching between the optical and microwave modes.

- Since the optical mode volume is so much smaller than the microwave we are limited by the microwave mode volume and win by making it smaller.
- The coupling is proportional to the electro-optic coefficient as expected but it also proportional to the square of the optical index of refraction so we win by going to high index of refraction materials (e.g. silicon).
- In addition to simple spatial overlap of the modes, we need to get phase matching as well. One can consider the beat mode of the two optical modes matching the microwave mode. In the ring traveling wave resonator this means we need the microwave mode to also have a 2π angular dependence.

The challenge in the SQOT program is to use the semi-lumped element qubit resonator's small mode volume but still keep the phase matching condition.

2.3.2 Numerics

As discussed above, the microwave-to-optical coupling strength depends on the microwave mode volume and the phase matching. We have numerically explored 8 possible SQOT designs (two designs without a Josephson junction for comparison). The device designs are shown in Figure 2.4.

These devices are designed to optimize the coupling strength with the frequency around 5 - 10 GHz. We first calculate the maximum achievable coupling for each device design which is defined by the microwave mode volume (or the qubit capacitance as stated in the proposal). The calculations are summarized in Table 1. This shows that the SQOT design with a qubit (junction resonator) can be designed to improve the maximum achievable coupling compared to the ring resonator and the coax cavity as the inductance of the junction allows for a smaller mode volume.

To finalize the coupling strength, we need to calculate the phase matching between the microwave and the optical mode by evaluating the mode overlap (E-field) integral between

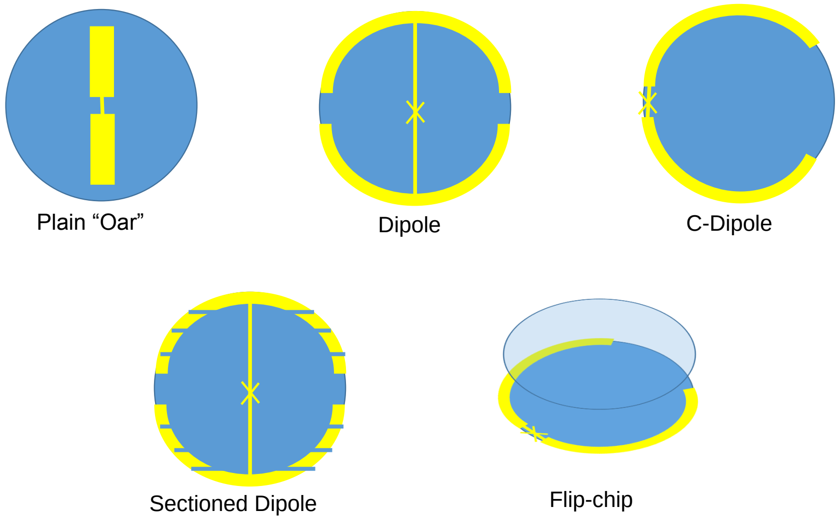

Figure 2.4: Different designs for the SQOT device that were simulated in HFSS. Starting from the standard oar design; then a modified oar dipole to match the optical mode; the C-dipole concentrates more of the optical mode at the edges of the disk; the sectioned dipole attempts to reduce the capacitance to keep the qubit frequency up; finally a flip-chip solution that works around fabrication on $LiNbO_3$ difficulties (see Sec. 3.2).

the two modes. Despite extensive effort the mixed-physics of optics and microwaves proved challenging to integrate. It is quite challenging to simulate the E-field in HFSS with a fine enough resolution (< 0.1 micron) on the scale of the optical mode cross section yet in a large physical volume (optical cavity perimeter ≈ 10000 microns) such that the numerical integration converges. A calculation from existing literature [7] shows that the maximum phase matching factor between a microwave ring resonator and an optical WGM can be 0.5 which gives us an estimate for the actual coupling rate. A potential work around is to use the 3-D microwave field simulation results from HFSS for various SQOT designs and an analytically calculated whispering gallery optical mode at 1550 nm to numerically evaluate the mode overlap integral.

3 EXPERIMENT

3.1 $LiNbO_3$ LOSS MEASUREMENT

The low-temperature dielectric loss tangent of $LiNbO_3$ had not been reported when the SQOT program started and it is one of the most important metrics to obtain to gauge the feasibility of our approach. We started with our conventional measurment technique using an ultra high-Q cylindrical resonator, fitting the spectrum and using HFSS models of the resonance to determine the filling factor. Our first results showed that the microwave loss bound could be $< 10^{-3}$ which was much higher than initially expected so we switched to a superconducting aluminum rectangular cavity whose internal Q is about 5×10^{-6}.

The advantage of using a rectangular cavity is the order of magnitude lower density of resonant modes within our measurement band (4 - 12 GHz) compare to the cylindrical cavity, which makes it easier to identify the relevant mode that contains the information of the $LiNbO_3$ microwave loss which will depend on a participation ratio. A $LiNbO_3$ chip was diced in a 2 mm X 6.8 mm size and the cavity frequency with the $LiNbO_3$ chip is 11.886 GHz. In our first measurement that was done in a transmission configuration with two ports, we set two nearly identical couplers at a moderate strength with an insertion loss of 60 dB at room temperature.

We performed three experimental scans:

1. Bare cavity measurement
2. Power dependence of the resonant width
3. Temperature dependence of the resonant width

on two different $LiNbO_3$ samples. The bare cavity Q was 65,000 which is likely to be limited by the coupling Q. After this measurement, we put the $LiNbO_3$ chip in the same cavity and cooled-down the device to measure power and temperature dependence of the resonant width. The inferred loss tangent ranges from $\tan\delta \approx 1.1 \times 10^{-4}$ ($Q \approx 9000$) when the loaded Q is entirely from the internal loss of the $LiNbO_3$, to $tan\delta \approx 9 \times 10^{-5}$ ($Q \approx 11100$). We calculated the coupling Q by simulating the exact cavity setup in HFSS. Even with the same coupling setup, the coupling Q of the bare cavity and the cavity with the substrate are different since the substrate stores more electric-field energy. Moreover, the thermal contraction of the whole cavity setup gives a different coupling Q at low temperature from the room temperature value. Knowing the internal Q of the bare cavity from previous measurements, we compared the measured bare cavity Q and the simulation to obtain the exact configuration of the couplers and simulated the cavity again with the substrate to retrieve the coupling Q for our loss tangent measurement setup.

Figure 3.1 shows the cavity resonance with $LiNbO_3$ measured at various temperature stages from 0.015 K to 2 K. There are a few noticeable features shown in the peaks, consistently throughout all temperature stages. We could not find any previous literature relating this to any nonlinearity of $LiNbO_3$. However, private communication and an arXiv publication at the end of the SQOT program [8] shed some light. Impurities in $LiNbO_3$ can have zero field splitting at 11GHz. This same work reported a loss tangent "of order 10^{-5}" with no further details but appears to be consistent with our findings. Note that in our loss tangent measurement setup, the electric-field was aligned with the X axis of $LiNbO_3$ while the measurement from the recent literature [8] measured the loss tangent along the Z-axis which may explain the discrepancy in loss tangent numbers between Ref. [8] and us.

The resonant width did not show any measurable dependence on temperature, except at 1.23K which is the superconducting transition temperature of aluminum. The temperature dependence of the $LiNbO_3$ quality factor could hint us the loss mechanism of $LiNbO_3$ if it is intrinsic (phonon-limited) or extrinsic (defect-limited). If it is intrinsic, the Q will follow a specific temperature dependence while if it is defect limited it will bottom out when limited by the defects. However, the resonance width also did not show much power-dependence which we expected to happen since a power-dependent behavior is typical to any nonlinear effect. We were not able to extend the results to the very low power regime to a poor signal-to-noise ratio but recent work [8] did not show any power dependence down to the single photon level.

We performed two additional cool-downs to confirm the Z-cut $LiNbO_3$ loss-tangent and also measured an X-cut wafer. The electric-field was aligned with the X-axis of the $LiNbO_3$. We used a different piece of $LiNbO_3$ and the microwave loss was measured with one port to reduce the number of unknowns from the port coupling Q. In all cases we found that the loss tangent of $LiNbO_3$ was similar to the previous measurements which was $\tan\delta \approx 1 \times 10^{-4}$.

3.2 Qubit Fabrication on $LiNbO_3$

The microfabrication of a small Josephson junction on a Z-cut $LiNbO_3$ substrate was one of the most difficult challenges, as we expected from the beginning of the SQOT program, due to its piezo- and pyroelectricity. For example, resist baking (increasing temperature to 180C) can cause sufficient electron-discharging and thermal shock to break the device. The fabrication yield has not been as good as our typical 3D process on sapphire. Thus, in parallel with the fabrication effort on $LiNbO_3$, we decided to try a flip-chip approach to improve the yield where a superconducting qubit is fabricated on a sapphire chip with our well-established fabrication recipe and we put the sapphire chip with the qubit on top of $LiNbO_3$ for electro-optic coupling. HFSS device simulations showed a similar level of the microwave E-field in the $LiNbO_3$ WGM resonator, so this could be an alternative solution.

To further test this possibility we ran multiple tests of the flip-chip configuration's effect on the qubit coherence. In particular we wanted to answer:

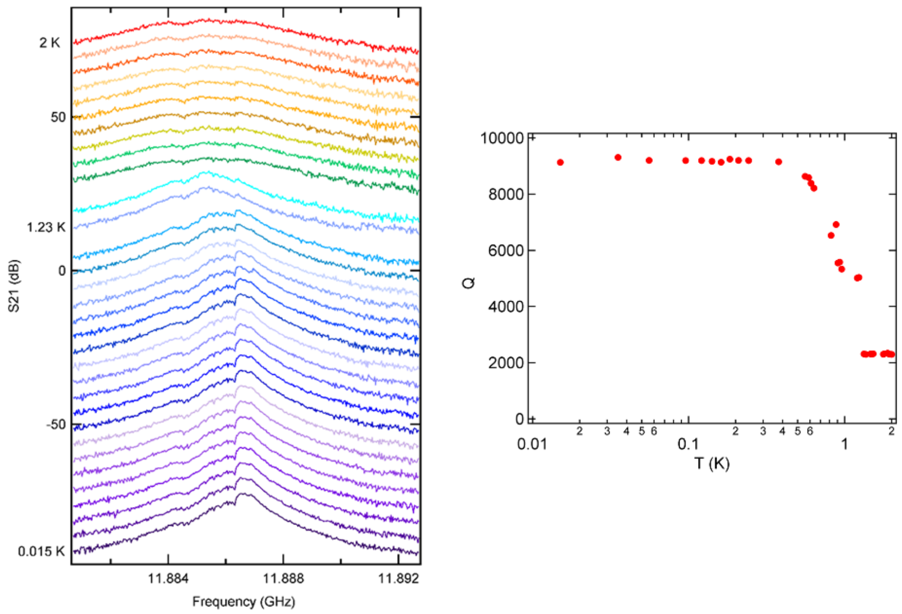

Figure 3.1: Resonant peaks of the superconducting microwave cavity with $LiNbO_3$ wafer present and the resonant width (loaded Q) vs temperature obtained from a simple Lorentzian fit.

1. If the Josephson junctions will survive with a substrate on top?
2. How large the vacuum gap is between two sapphire substrates?
3. If T_1 will remain the same in the flip-chip configuration?

We used a previously measured 3D qubit device with $T_1 \approx 100\mu$s. The configuration (as an HFSS model) is shown in Figure 3.3. For this initial testing, we used a recycled blank sapphire where a junction was previously patterned and physically removed. We performed four individual cool-downs to measure T_1 of the same device but in each cool-down, we changed the flip-chip configuration to understand the effect of the blank sapphire. The results are summarized in Table 1. With a blank substrate facing the qubit, the qubit survived but T_1 decreased significantly by a factor of 4-5 compared to the cases where the substrate was not facing the qubit which strongly suggests an additional surface loss from the flip-chip. Our HFSS simulation shows the vacuum gap between two sapphire pieces should be less than 10 microns but calculating the actual thickness of the vacuum gap will require more intense HFSS simulation studies.

For fabrication directly on $LiNbO_3$ we found that the wafers broke easily during e-beam resist baking due to the $LiNbO_3$'s pyroelectricity and we had difficulty completing the fabrication process. The mitigation approach taken was to use a programmable oven for the resist baking that can raise the temperature slowly by 1 degree C per minute to prevent the thermal shock. With the programmable oven, we were able to complete the fabrication process. Unfortunately, we still have no live junctions fabricated on $LiNbO_3$ and only had either short or open which

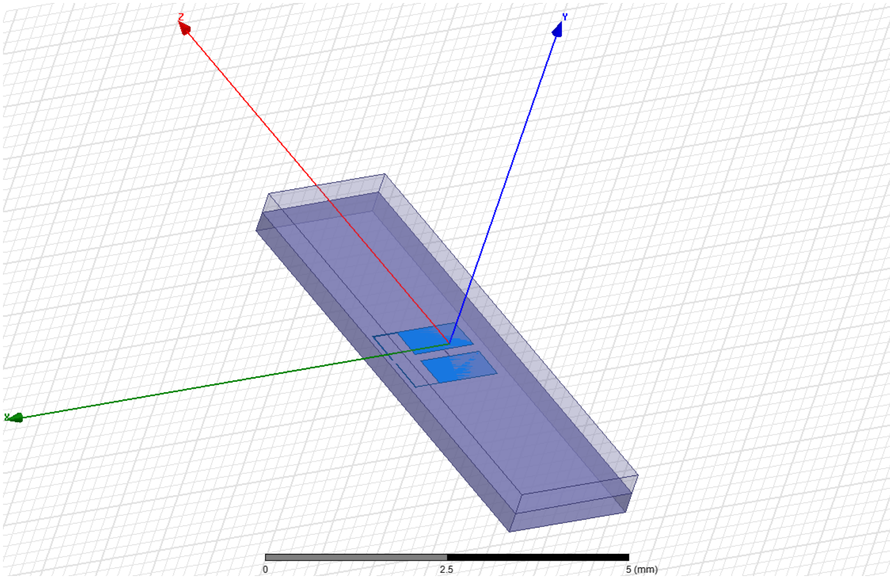

Figure 3.2: HFSS model of the flip-chip testing. A blank piece of sapphire is laid on top of 3D qubit fabricated on a second sapphire substrate.

Setup	T_1 (μs)
Previously measured	100
Sapphire substrate on top	13
Sapphire substrate below	80
Removed sapphire	60

Table 3.1: T_1 measurements on a sapphire-sapphire flip-chip 3D qubit. The measurement was done on the same 3D qubit but with a different flip-chip configuration. The time order of each measurement is from top to bottom.

we think had happened due to electrostatic discharge (ESD) again from the pyro/piezo-electric properties of $LiNbO_3$.

To mitigate the ESD issue we deposited a thin niobium (Nb) metal layer before fabricating the junctions and then selectively chemically etch the Nb using XeF_2 after the junction is formed on the Nb. The selective etch from XeF_2 will not affect aluminum junctions and will be able to remove Nb film underneath the junction such that the device will not be shorted due to the Nb film. We are currently processing another $LiNbO_3$ wafer and fabricating junctions using this recipe.

The recipe below successfully fabricated aluminum junctions on a Z-cut $LiNbO_3$ wafer.

1. Wafer cleaned with solvents, acetone, IPA and blow dry.
2. Spin-coat on portable spinner in offline lab. This was to accommodate baking in a programmable oven. Standard spin conditions for MMA.
3. Bake in programmable oven: 1 degree C per minute ramp up to 170C; dwell time 10 minutes; then ramp down at 1 degree C per minute. This step takes approximately 4 hours total.
4. Remove from oven and spin-coat PMMA and bake with same conditions in previous step.
5. Remove from oven and evaporate 10nm Al as a discharge layer for ebeam.
6. Expose in e-beam.
7. Remove the Al in OPD7262 (TMAH based) and then develop in MIBK:IPA 1:3 solution and rinse in IPA room temp. These develop conditions gave better results then cold develop.
8. Create aluminum oxide junction in LESKER tool using standard conditions and then liftoff in Acetone and rinse and dry.

While the junction resistances indicated good qubits at room temperature, we have not yet been able to test the qubits cold as none have survived the thermal cycle of being cooled in the dilution fridge.

3.3 Optical Coupling the $LiNbO_3$ WGM Resonator

Achieving over-coupling to the optical resonator is crucial to ensure that all the photons carrying quantum information leak out into the collection path rather than being dissipated in internal losses and it proved challenging to design an approach compatible with a dilution fridge requirement. The coupling presents several difficulties:

1. the high Q optical resonator has a very tightly confined optical mode with very little evanescent field to couple to;

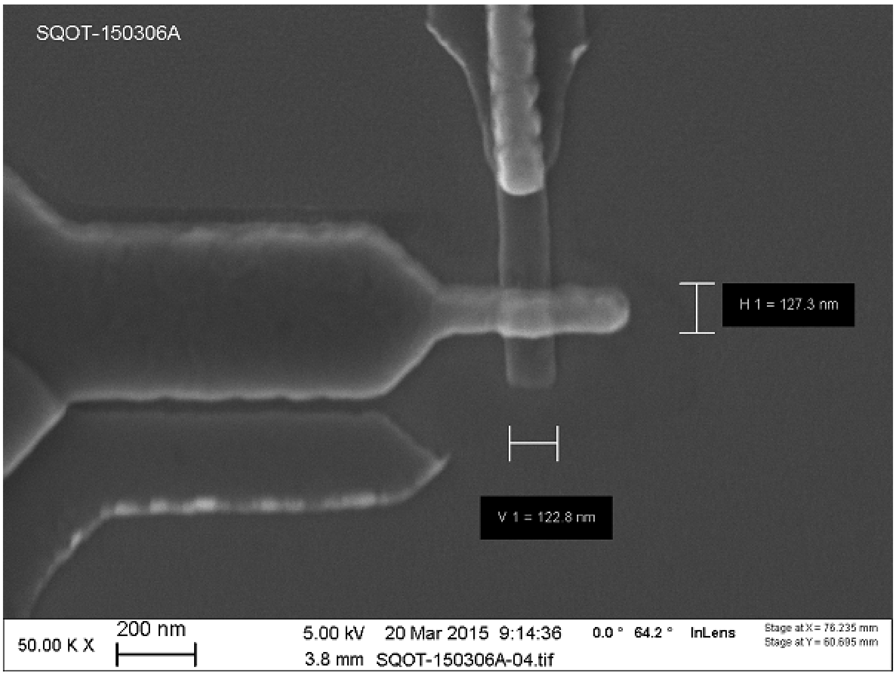

Figure 3.3: SEM image of a live aluminum junction fabricated on Z-cut $LiNbO_3$ wafer. To prevent ESD, the junction was fabricated on a Nb layer which was removed by XeF_2 after the junction was formed.

2. the high (relative to conventional glass fibres) index of refraction makes phase matching difficult;

3. the whispering gallery mode disk is a traveling wave mode resonator with both an input and output port.

3.3.1 Failed approach: prism coupling

The proposed approach was to use the conventional room temperature prism coupler. By tuning the angle of total internal reflection at the prism wall the effective phase velocity along the tangent direction to the disk can be adjusted. With a sufficient number of degrees of freedom in the input coupler and output coupler, it is possible to get the beam aligned with the disk; incident at the optimal angle and have the optimal prism-disk spacing to achieve the desired coupled Q. However an initial engineering analysis showed that this approach would be too fragile at cryogenic temperatures. The changes in index of refraction with temperature and thermal contraction would force us to have an infeasibly number of motion stages at the base of the dilution fridge.

3.3.2 Failed approach: $LiNbO_3$ waveguides

An academic group had reported some success in using waveguides defined in $LiNbO_3$ [9]. The waveguides are defined by patterned doping of the $LiNbO_3$ wafer. This approach was also promising because $LiNbO_3$ waveguides are used in conventional room-temperature electro-optic modulators so commercial vendors were available that had some limited cryogenic experience. Unfortunately, a more careful analysis and simulation showed why the academic group was under-coupled to the resonator. There are two key issues with this approach

1. The high index of refraction of $LiNbO_3$ means most of the energy that leaks from the waveguide mode stays in the surrounding $LiNbO_3$ substrate - not into the air above the waveguide where it can couple into the disk.

2. The waveguide and disk are not well phase-matched because the effective index two modes are pushed in opposite directions: the WGM mode is slightly below $LiNbO_3$ where as the waveguide mode must be higher (from the doping) to enable confinement in the substrate.

3.3.3 Taken approach: silicon waveguides

Bringing addition integrated photonics expertise to the team at both IBM and BBN enabled a new approach that is also compatible with future more integrated devices. The difficulty of coupling to a high index of refraction resonator with fibre had been noted in the literature and the silicon waveguide solution was speculated about: “When the resonator is made of lithium niobate or diamond, for example, it is not trivial to make a phase-matched taper, though the planarized silicon waveguide would likely do the trick." [10]. Indeed with appropriate dimensions silicon waveguides can be index matched to the whispering gallery mode. Silicon

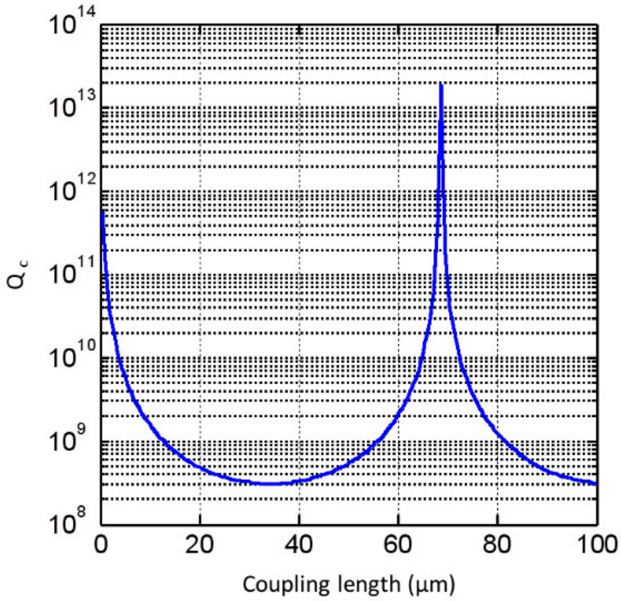

Figure 3.4: Coupled Q for a $LiNbO_3$ waveguide coupled to a $LiNbO_3$ disk WGM. The periodic dependence with coupling length comes from coherent exchange of energy back and forth between the two modes. The minimum Q is far above the intrinsic Q of the WGM showing the approach remains in the under-coupled regime.

has a higher index of refraction than $LiNbO_3$ but if the waveguide is made thin enough a substantial enough portion of the mode will live above the waveguide in air and the effective index of refraction will be lowered. This squeezing of the mode out of the waveguide also helps get good coupling into the whispering gallery mode. Silicon waveguides are more lossy than $LiNbO_3$ but that will not be a limiting factor.

Finite element simulations confirmed the above intuition and showed optical over-coupling to the disk should be possible for a range of disk-waveguide gaps (see Figure 3.3.3). The effective coupling can be tuned by adjusting the waveguide-disk distance via a piezo-translation stage or the length of of the interaction region.

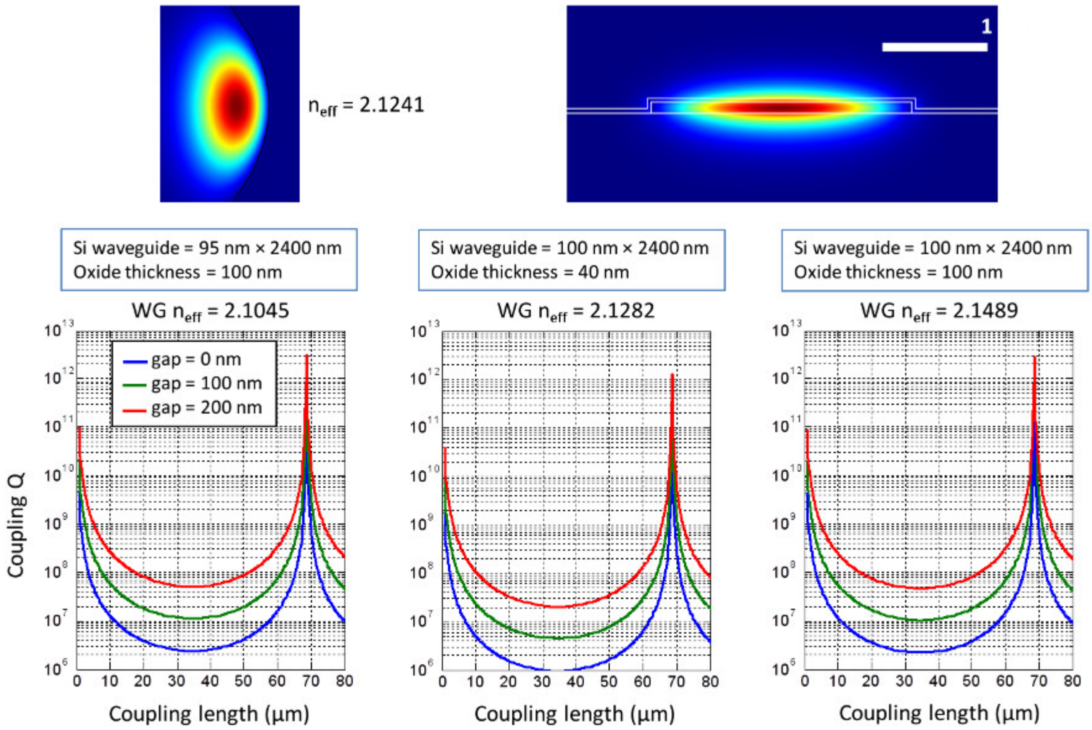

Figure 3.5: Coupling Q for a Si waveguide coupled to a $LiNbO_3$ disk WGM with various dimensions and protective oxide thicknesses. The coupled Q can reach the over-coupled regime for certain gaps and interaction regions. The interaction region can be set by patterning a U in the waveguide.

Si waveguides were fabricated with the following procedure:

1. We started the fabrication process on SOI wafers from Soitec. The wafer has a Si thickness of 250 nm and underneath oxide thickness of 3 microns.

2. We first thin down the Si layer to 100 nm thickness. For this process we use thermal oxidation of Si and then wet etching of the grown oxide.

3. All the waveguide pattern of various dimensions (widths and U shapes) were defined by e-beam lithography and using Zep520A electron resist.
4. The e-beam written patterns were etched in an inductively-coupled plasma (ICP) etching machine with and etch recipe that we developed for waveguide fabrication.
5. After the etching, the wafer was diced in to chips.
6. For sanity check, the fabricated chips were inspected and imaged using scanning electron microscopy (SEM)
7. Then using diamond polishing equipment, the input and output facet (edge) of each chip was polished in order to efficiently couple the laser light into/out-of the chip.

A variety of dimensions were written in the mask for testing and sweeping design parameters. The waveguides were tapered from the thin rectangular cross section in the interaction region to a square for fibre coupling into and out of the chip. For initial testing the chip facets were polished back to the waveguide section but future interaction will include and deep groove etch for mounting the fibres. We were unable to complete optical testing and validation of the waveguides however we are exploring options to fund this effort through internal investment at BBN.

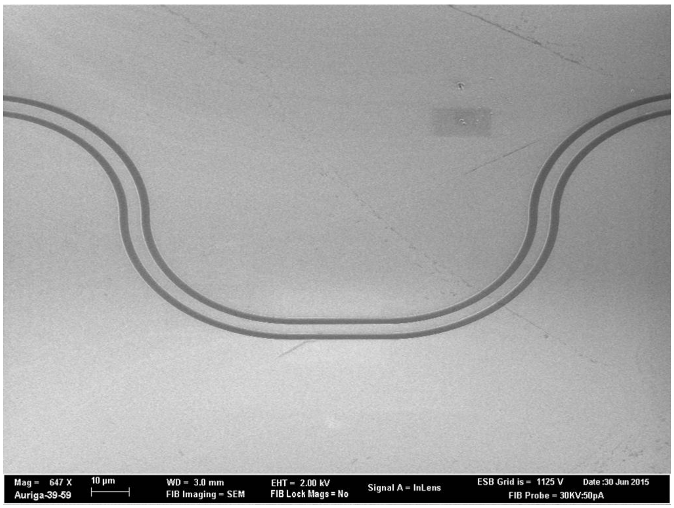

Figure 3.6: SEM micrograph of a section of fabricated Si waveguide for coupling to a $LiNbO_3$ disk.

4 Technical Feasibility

The physics of the electro-optic effect, whose technology has been successfully adopted in classical information processing, also offers an attractive approach in quantum information processing to directly convert between microwave photons and optical-frequency photons with less hardware requirement and fewer engineering challenges that may enable a faster and more effective microwave-optical conversion than most of other conversion technologies have. In this approach, two key figures of merit, the conversion rate and efficiency, highly depend on the material properties such as the electro-optic coefficient (or a $\chi^{(2)}$ nonlinearity) and optical or microwave loss tangent. Therefore, to successfully harness the advantages of the electro-optic technology for quantum applications, selecting a good electro-optic material is extremely crucial.

In the SQOT program, we investigated the technical feasibility of the electro-optic approach using $LiNbO_3$ to build a quantum transducer for superconducting qubits. As the most commonly used electro-optic material for the classical communication applications, $LiNbO_3$ has some advantages with its high electro-optic coefficient and high optical quality factor. However, its high cryogenic microwave loss and strong pyroelectricity along with other non-linear effects makes $LiNbO_3$ not the most optimum choice to utilize for quantum microwave-optical transduction.

For the electro-optic approach to be technically feasible to realize a quantum microwave to optical transducer for superconducting quantum computing, the following conditions must be considered:

1. The electro-optic material should exhibit a high-quality factor at both microwave and optical frequencies as well as a strong electro-optic effect at cryogenic temperatures, without any other strong non-linear effect coexisting. Materials with an engineered electro-optic property could be a good alternative candidate. For example, Si with an engineered electro-optic effect induced by a straining material is an appealing choice to consider since Si is known to show a high-quality factor at both microwave and optical frequencies. However, more material studies need to be done to understand the electro-optic effect on Si.

2. A proper isolation mechanism between the microwave part and the optical part must be engineered. The isolation should be sufficient to prevent any plasmonic loss caused by superconducting parts on optical signals and any quasiparticle loss caused by optical photons on microwave signals. Using a superconducting 3D cavity as the microwave device can be a good option to exert enough electric-fields to the electro-optic material without making a direct contact which may minimize both the plasmonic and quasiparticle losses.

3. The electro-optic material should be easily integrable with superconducting circuits. A fully integrated photonic device discussed in Sec. 3.3.3 is a good approach. The integrated photonic device is not only compatible with superconducting qubit fabrication but also enables good optical alignment at cryogenic temperature.

4. The device must support a hierarchy of timescales: coversion rate faster than cavity-transmission line coupling faster than loss rates in order to generate high-quality entanglement.

Through SQOT, our team achieved several new results in the field of quantum electro-optics investigating the possibility of the electro-optic approach to realize quantum signal transduction between microwave and optics. Our team made one of the first measurments of the loss tangent of $LiNbO_3$ at a dilution fridge temperature. For the first time, aluminum superconducting Josephson junctions were fabricated on $LiNbO_3$ via the SQOT program. All challenges we tackled through SQOT were unprecedented. We believe that further material studies on electro-optic materials at cryogenic temperature will open more opportunities to utilize electro-optic physics, the studies from SQOT inspired us to think about a future direction of a more integrated platform for electro-optic devices and will benefit the community to explore unconventional and different directions.

References

[1] Mankei Tsang. "Cavity quantum electro-optics". In: *Physical Review A* 81.6 (June 2010), p. 063837. ISSN: 1050-2947. DOI: 10.1103/PhysRevA.81.063837. URL: http://link.aps.org/doi/10.1103/PhysRevA.81.063837.

[2] Mankei Tsang. "Cavity quantum electro-optics. II. Input-output relations between traveling optical and microwave fields". In: *Physical Review A* 84.4 (Oct. 2011), pp. 1–8. ISSN: 1050-2947. DOI: 10.1103/PhysRevA.84.043845. URL: http://link.aps.org/doi/10.1103/PhysRevA.84.043845.

[3] R. W. Andrews et al. "Bidirectional and efficient conversion between microwave and optical light". In: *Nature Physics* 10.4 (Mar. 2014), pp. 321–326. ISSN: 1745-2473. DOI: 10.1038/nphys2911. arXiv: 1310.5276. URL: http://arxiv.org/abs/1310.5276%20http://www.nature.com/doifinder/10.1038/nphys2911.

[4] C. Eichler et al. "Observation of Entanglement between Itinerant Microwave Photons and a Superconducting Qubit". In: *Physical Review Letters* 109.24 (Dec. 2012), p. 240501. ISSN: 0031-9007. DOI: 10.1103/PhysRevLett.109.240501. URL: http://link.aps.org/doi/10.1103/PhysRevLett.109.240501.

[5] Andreas Reiserer and Gerhard Rempe. "Cavity-based quantum networks with single atoms and optical photons". In: (2014), pp. 1–42. arXiv: 1412.2889. URL: http://arxiv.org/abs/1412.2889v1.

[6] John E. Gough and Guofeng Zhang. "Generating Nonclassical Quantum Input Field States with Modulating Filters". In: *arXiv preprint arXiv:1404.3866* 1 (2014), pp. 1–4. arXiv: arXiv:1404.3866v1. URL: http://arxiv.org/abs/1404.3866.

[7] AA Savchenkov and AB Matsko. "Single-sideband electrooptic modulators and their application in tunable opto-electronic oscillators". In: *Microwave Photonics, 2009. MWP '09. International Topical Meeting on* (2009), pp. 2–5. URL: http://ieeexplore.ieee.org/xpls/abs%5C_all.jsp?arnumber=5342730.

[8] Maxim Goryachev, Nikita Kostylev, and Michael E Tobar. "Single Photon Level Study of Microwave Properties of Lithium Niobate at milli-Kelvin Temperatures". In: *arXiv* (2015), p. 1504.07352. arXiv: 1504.07352v1.

[9] D. Farnesi et al. “Coupling light to whispering gallery mode resonators”. In: 9133 (May 2014). Ed. by Laurent Vivien et al., p. 913314. DOI: 10.1117/12.2057611. URL: http://proceedings.spiedigitallibrary.org/proceeding.aspx?doi=10.1117/12.2057611.

[10] L. Maleki et al. “Crystalline Whispering Gallery Mode Resonators in Optics and Photonics”. In: *Practical Applications of Microresonators in Optics and Photonics*. 2009. ISBN: 9781420065787.